

Quantifying the Cosmic Web I: The large-scale halo ellipticity-ellipticity and ellipticity-direction correlations

Jounghun Lee^{1*}, Volker Springel², Ue-Li Pen³, and Gerard Lemson^{4,5}

¹*Department of Physics and Astronomy, FPRD, Seoul National University, Seoul 151-747, Korea*

²*Max-Planck-Institute for Astrophysics, Karl-Schwarzschild-Str. 1, D-85741 Garching, Germany*

³*Canadian Institute for Theoretical Astrophysics, Toronto, ON M5S, Canada*

⁴*Astronomisches Rechen-Institut, Zentrum für Astronomie der Universität Heidelberg, Mönchhofstr. 12-14, 69120 Heidelberg, Germany*

⁵*Max-Planck Institut für extraterrestrische Physik, Giessenbach Str., 85748 Garching, Germany*

Accepted 2007 ???. Received 2007 ???; in original form 2007 September 10

ABSTRACT

The formation of dark matter halos tends to occur anisotropically along the filaments of the Cosmic Web, which induces both ellipticity-ellipticity (EE) correlations between the shapes of halos, as well as ellipticity-direction (ED) cross-correlations between halo shapes and the directions to neighboring halos. We analyze the halo catalogue and the semi-analytic galaxy catalogue of the recent Millennium Run Simulation to measure the EE and ED correlations numerically at four different redshifts ($z = 0, 0.5, 1$ and 2). For the EE correlations, we find that (i) the major-axis correlation is strongest while the intermediate-axis correlation is weakest; (ii) the signal is significant at distances out to $10 h^{-1}\text{Mpc}$; (iii) the signal decreases as z decreases; (iv) and its behavior depends strongly on the halo mass scale, with larger masses showing stronger correlations at large distances. For the ED correlations, we find that (i) the correlations are much stronger than the EE correlations, and are significant even out to distances of $50 h^{-1}\text{Mpc}$; (ii) the signal also decreases as z decreases; (iii) and it increases with halo mass at all distances. We also provide empirical fitting functions for the EE and ED correlations. The EE correlations are found to scale linearly with the linear density correlation function, $\xi(r)$. While the ED cross-correlation is found to scale as $\xi^{1/2}(r)$ at large distances beyond $10 h^{-1}\text{Mpc}$. The best-fit values of the fitting parameters for the EE and the ED correlations are all determined through χ^2 -statistics. Our results may be useful for quantifying the filamentary distribution of dark matter halos over a wide range of scales.

Key words: methods:statistical – cosmology:theory – galaxies:clustering – galaxies:halos – large-scale structure of Universe

1 INTRODUCTION

One of the most striking features of the Universe is that the observed distribution of galaxies on large scales shows a web-like filamentary pattern, which is often called the “Cosmic Web”. Recent large N-body simulations of the cold dark matter cosmology demonstrated vividly the geometric richness of the filamentary web that spatially connects the dark matter halos, and which directly relates to the structure seen in the galaxy distribution. One of the most fundamental tasks in cosmology is thus to establish a physical model for the filamentary cosmic web and to quantitatively explain its global properties.

The existence of the filamentary web was originally

predicted by the top-down scenario of the hot dark matter (HDM) model (Zel’dovich 1970). If cosmic structures form through top-down fragmentation, then one- and two-dimensional collapse of matter would naturally lead to the formation of sheet-like and filamentary structures on large scales. Therefore, it was regarded first as a mystery why and how the filamentary web came into being also in a cold dark matter (CDM) dominated universe.

A breakthrough was made by Bond et al. (1996) who developed a cosmic web theory that can explain the presence of a filamentary web in the CDM cosmogony. This theory explains that the filamentary web can occur naturally in the CDM dominated universe due to the coherent nature of the primordial tidal field. The filamentary web is in fact a manifestation of the primordial tidal field sharpened by nonlinear effects. The cosmic web theory has provided a

* E-mail:jounghun@astro.snu.ac.kr

standard framework within which the formation of cosmic large-scale structure can be qualitatively understood. Yet, it is still quite difficult to describe the cosmic web quantitatively both in theoretical and in observational terms. Theoretically, the inherent anisotropic nature and geometrical complexity of the cosmic web makes it complicated to fully characterize its statistical properties. Observationally, it is hard to trace the filamentary structures from observational data, since there is no well-established way to identify them.

In spite of these difficulties, various methodologies and algorithms have already been suggested to quantify the filamentary structures: Higher-order N-point statistics has been used to describe the anisotropic matter distribution in a cosmic web (Croton et al. 2004; Kulkarni et al. 2007); the percolation statistics was used to characterize the filamentary shapes of the large-scale structures (Sahni et al. 1997; Shandarin & Yess 1998); the skeleton formalism has been developed to extract the filamentary structures from a three dimensional density field (e.g., Sousbie et al. 2007, and references therein); the Minimal-Spanning-Tree algorithm has been introduced to find the basic structural elements of the cosmic web (Colberg 2007).

Although the above methods are quite useful for determining the overall filamentary structure of the cosmic web, these approaches are largely phenomenological without accounting for the physical mechanism for the formation of the cosmic web. According to the theory proposed by Bond et al. (1996), the filamentary web originated from the large-scale coherence of the primordial tidal field and its sharpening by nonlinear effects during structure growth. Part of this nonlinear sharpening effect arises from the gravitationally driven merging of halos and the infall of matter, which preferentially occurs along the most prominent filaments. This increases the anisotropy in the halo clustering and thus sharpens the filamentary web.

To describe the cosmic web quantitatively in terms of its underlying physical principles it will be necessary to account for the effects of the tidal field and the anisotropic merging along filaments. The tidal field causes intrinsic alignments of the principal axes of the dark halos in the cosmic web (Croft & Metzler 2000; Heavens et al. 2000; Catelan et al. 2001; Jing 2002; Hui & Zhang 2002; Lee & Pen 2007), while anisotropic merging induces elongation of the major axes of the halos along prominent filaments (West 1989; West et al. 1991). As a result, there exist spatial correlations between the halo ellipticities (EE correlations), and cross-correlations between the halo ellipticities and the large-scale density field (ED cross-correlations). Hence, one can view the observed filamentary web as a large-scale manifestation of the EE and ED correlations, which are in turn induced by the effects of the tidal field and the anisotropic merging.

The goal of this paper is to quantify the filamentarity and the typical scales of the cosmic web in terms of the EE and ED correlations. This is also highly important for assessing to what degree these correlations can systematically bias weak gravitational lensing mass reconstructions and cosmological parameter estimates based on cosmic shear measurements. In fact, the ED cross-correlations have become a hot issue in the weak lensing community, since it has been realized that they could mimic weak lensing signals at a significant level (Hirata & Seljak 2004; Mandelbaum et al. 2006; Hirata et al. 2007).

Several authors have already studied numerically the EE and ED correlations. Hopkins et al. (2005) examined the evolution of cluster alignments by using a large-scale N-body simulation. Altay et al. (2006) have shown from high-resolution N-body data that the alignments of clusters are strongly related to the existence of the connecting filaments. Heymans et al. (2006) explored the possible correlations between the weak lensing shear and the orientation of foreground galaxies by analyzing N-body simulation. Here in our work, we measure both the EE and ED correlations at large distances by using the Millennium dataset and describe quantitatively their scalings with distance, mass, as well as redshift.

The organization of this paper is as follows. In Section 2, we describe the N-body dataset we use and explain how we measure halo ellipticities from the N-body simulation and its associated galaxy catalogue. In Sections 3 and 4, we report numerical detections of the EE correlations and the ED cross-correlations, and examine how the signals depend on distance scale, redshift and halo mass. We also provide useful fitting formula for them. Finally, in Section 5, we summarize the results and discuss the implications of our work.

2 SIMULATION DATA AND METHODOLOGY

Our analysis is based on the halo catalog and the semi-analytic galaxy catalog from the recent high-resolution *Millennium Simulation*¹, which followed 10^{10} dark matter particles in a Λ CDM concordance cosmology (Springel et al. 2005). The size of the periodic simulation box is $500 h^{-1}$ Mpc and each dark matter particle in the simulation has a mass of $8.6 \times 10^8 h^{-1} M_{\odot}$. The basic cosmological parameters of the simulation were chosen as $\Omega_m = 0.25$ (the mass density); $\Omega_{\Lambda} = 0.75$ (the vacuum energy density); $h = 0.73$ (the dimensionless Hubble constant); $\sigma_8 = 0.9$ (the linear power spectrum amplitude); and $n_s = 1$ (the slope of the primordial power spectrum).

As part of the analysis of the Millennium run, halos of dark matter particles were first identified with the standard friends-of-friends (FOF) algorithm, and then decomposed into gravitationally bound subhalos using the SUBFIND algorithm (Springel et al. 2001). Based on detailed merger trees constructed for the subhalos, the halos were then populated with luminous galaxy models using semi-analytic simulations of the galaxy formation process (Croton et al. 2006).

We here use the spatial distribution of subhalos and galaxies to characterize the shape of FOF halos, in analogy to the procedure applied to observational galaxy surveys (e.g., Mei et al. 2007). For each FOF halo, we locate the satellite galaxies belonging to it. Then, we measure their tensor (I_{ij}) of second order mass moments as

$$I_{ij} = \sum_{\alpha} m_{\alpha} x_{\alpha,i} x_{\alpha,j}, \quad (1)$$

where m_{α} is the luminosity (or, equivalently the stellar mass) of the α -th galaxy and \vec{x}_{α} is the position of the α -th

¹ The Millennium Simulation data are available at <http://www.mpa-garching.mpg.de/millennium>

galaxy measured from the center of the mass of the satellite galaxies. We restrict our analysis to FOF halos massive enough to contain more than five substructures. By diagonalizing I_{ij} , we determine the three principal axes (major, intermediate, and minor axes) of I_{ij} . This allows us to measure the correlations between the three axes of the FOF halos as a function of separation. The results of our measurements are presented in detail in Section 3.

Before turning to our results, it is worth to discuss how our methodology relates to other, previously applied methods to characterize the shape of halos. Note that we here do not use all dark matter particles of a FOF halo to measure I_{ij} . Instead, we only use the satellite galaxies (or substructures) as tracers of the shape. In general, measuring the shape of a halo is a somewhat ambiguous issue, where a number of different strategies have been applied in the literature, but no generally accepted standard procedure exists (see e.g. the discussion in Springel et al. 2004; Allgood et al. 2006). Part of the ambiguity in measuring halo shape stems from the fact that one cannot delineate the outer boundary of a halo in a clear-cut way. If all particles belonging to a FOF halo are used to measure I_{ij} , then the ellipticity of a halo may be overestimated because of the large weight of the most distant points on the major axis, while in contrast, if only those particles within a certain spherical radius are used to measure I_{ij} , then the ellipticity of the halo is likely underestimated.

We use satellite galaxies (or substructures) to measure I_{ij} , because this approach mimics observationally accessible procedures. We expect that this definition should give halo shapes similar to those measured with all dark matter particles, as substructure and galaxy density are tracers of the dark matter distribution (e.g., Agustsson & Brainerd 2006). We will explicitly test this below. Note that we focus on quantifying the filamentary web induced by the anisotropic orientations of the halo ellipticities; we are not really interested in the *magnitude* of the shape distortion itself. This means that we are less sensitive to the details of measuring halo shape compared with attempts to quantify the axis ratio of the halo shape.

To examine to what extent different measuring methods yield different halo ellipticities, we carry out a simple test: Using a total of 227 FOF halos from the ‘milli’-Millennium simulation, which is smaller test run of the main Millennium simulation with a box size of $62.5 h^{-1} \text{Mpc}$ (Springel et al. 2005), we measured the halo shapes with three different methods: (A) using galaxies weighted by luminosity; (B) using dark matter substructures weighted by mass; and (C) using all dark matter particles. Then, we calculate the distribution of the angles θ between the principal axes of the halo shapes determined by these three methods. Figure 1 compares methods A and C (top), and methods B and C (bottom), in both cases plotting the histogram of the angles between the halos’ major, intermediate, and minor axes (left, middle, and right panels, respectively). As can be seen, there is a strong peak at $\theta = 0$, demonstrating that the halo principal axes obtained by the three different methods A, B and C are strongly correlated with one another. This correlation is particularly robust for the major axis, which defines the primary orientation of the predominantly prolate halos.

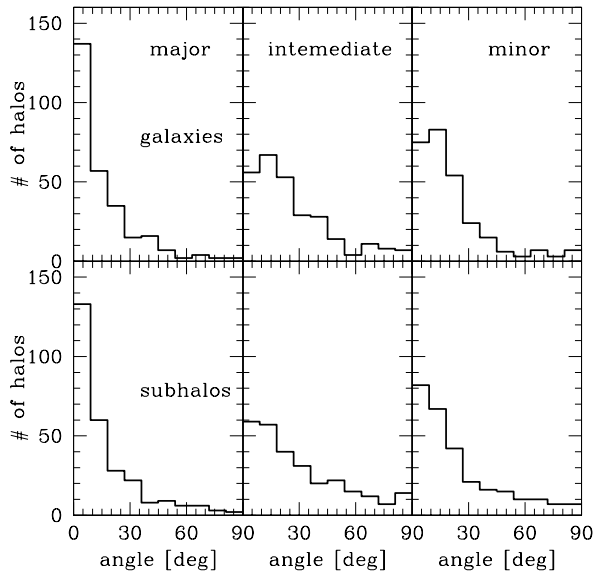


Figure 1. Distributions of the angles between the major, intermediate, and minor axes of the halos (left, middle, and right, respectively) from the milli-Millennium simulation, as determined by three different methods A, B, and C, which are based on the satellite galaxies, subhalos, and all particles belonging to the halos, respectively. The top-panels show the results from a comparison between the methods A and C, while the bottom panels give a comparison between the methods B and C.

3 THE HALO ELLIPTICITY-ELLIPTICITY CORRELATION

3.1 Definition

We define the EE correlation function, $\eta(r)$, as

$$\eta(r) \equiv \langle |\hat{\mathbf{e}}(\mathbf{x}) \cdot \hat{\mathbf{e}}(\mathbf{x} + \mathbf{r})|^2 \rangle - \frac{1}{3} \quad (2)$$

where $\hat{\mathbf{e}} \equiv (\hat{e}_i)$ represents the normalized eigenvector of a halo with unit magnitude. In eq.(2) the constant $1/3$ is subtracted since the first average term will yield $1/3$ in case that there is no EE correlation. Now that the three eigenvectors of each halo in the Millennium catalogs are all determined by the method described in Section 2, one can measure the EE correlations of the major (η_I), intermediate (η_{II}) and minor (η_{III}) principal axes separately as a function of the comoving distance r .

Basically, for each halo pair at a given redshift, we measure the separation distance r between the halo centers and calculate the squares of the dot products of the normalized eigenvectors of two halos. Then, we bin the radial distance r and calculate the mean values of $|\hat{\mathbf{e}}(\mathbf{x}) \cdot \hat{\mathbf{e}}(\mathbf{x} + \mathbf{r})|^2$ averaged over those halo pairs whose separation distances belong to a given bin, subtracting $1/3$ from it. We perform this procedure at $z = 2, 1, 0.5$ and 0 .

3.2 Evolution with redshift

Figure 2 plots the numerical results on the EE correlations measured at $z = 0, 0.5, 1$ and 2 in the top-left, top-right, bottom-left and bottom-right panels, respectively. In each

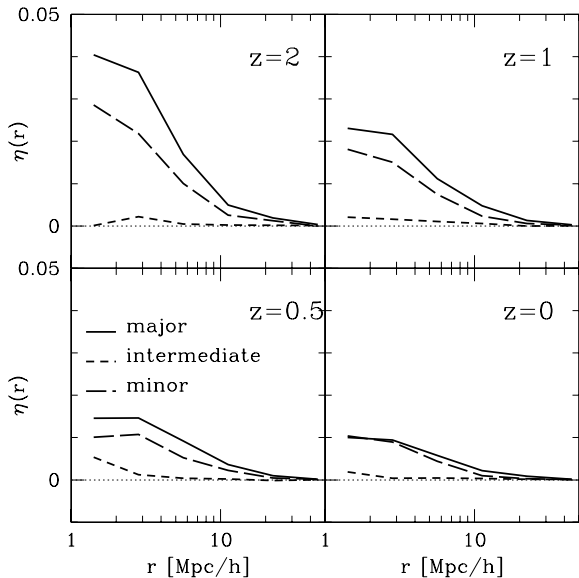


Figure 2. EE correlations of the halo major, intermediate, and minor axes (solid, dashed, and long dashed lines) at four different redshifts: $z = 0, 0.5, 1,$ and 2 (top-left, top-right, bottom-left, and bottom-right panel, respectively).

panel, the solid, dashed and long dashed lines represent $\eta_I(r)$, $\eta_{II}(r)$ and $\eta_{III}(r)$, respectively. The dotted line corresponds to the case of no correlation. As can be seen, the major-axis correlations are strongest and the intermediate-axis correlations are almost zero at all redshifts.

To see the behaviors of the EE correlations at large distances, we plot $\eta_I(r)$ and $\eta_{III}(r)$ as solid dots with errors σ_η in the logarithmic scale in Figs 3 and 4, respectively. In each panel the solid line represents the fitting model (see Section 3.4). For the estimation of σ_η , we divide the simulation volume into eight subvolumes each of which has a linear size of $250h^{-1}\text{Mpc}$ and measure the EE correlations in each subvolume separately. The errors, σ_η , are calculated as the standard deviation between realizations. This estimation of errors accounts for both the cosmic variance and the Poisson noise. It is also found that there exist non-negligible correlations between radial bins at distance larger than $5h^{-1}\text{Mpc}$ (see Section 3.4).

As can be seen, the EE correlations are strongest at $z = 2$, and exist out to distances of $10h^{-1}\text{Mpc}$. As z decreases, the correlations tend to decrease monotonically at all distance scales, indicating that the directions of the halo major and the minor axes tend to become randomized as z decreases. This result is consistent with the previous results obtained by Hopkins et al. (2005). The numerical results on the EE correlations measured at $z = 0$ are listed in Table 1.

3.3 Variation with mass

To study how the EE correlations scale with halo mass, we measure $\eta_I(r)$ from two different mass bins with the mass threshold $M_c = 1.42 \times 10^{13}h^{-1}M_\odot$ at $z = 0$. Table 2 lists the numerical results and Figure 5 plots $\eta_I(r)$ at $z = 0$ mea-

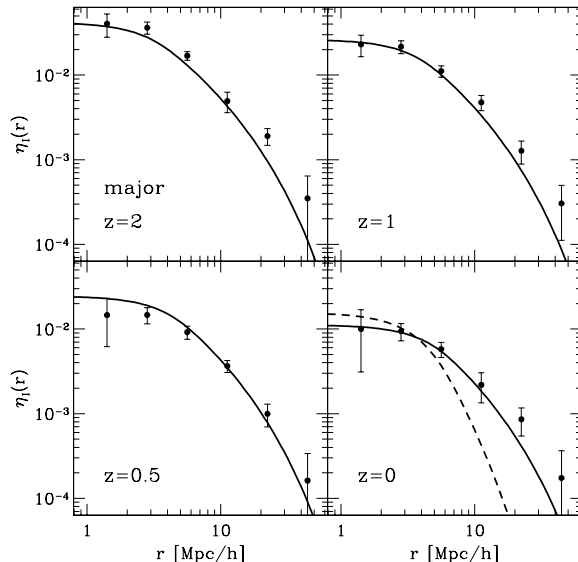


Figure 3. The EE correlations of the halo major axes at $z = 0, 0.5, 1$ and 2 . The errors, σ_η , represent the standard deviation between 8 realizations that are obtained from the subdivision of the simulation box. The errors do not include the correlations between radial bins. In each panel the solid line represents the fitting model (eq.3) proportional to the linear density correlation function, $\xi(r)$. In the bottom-right panel, the dashed line represents another fitting model proportional to $\xi^2(r)$.

Table 1. Numerical results on the EE correlations of the halo major (η_I) and the minor axes (η_{III}) in logarithmic scale measured at $z = 0$.

$\log[r/(h^{-1}\text{Mpc})]$	$\eta_I(r) \times 10^2$	$\eta_{III}(r) \times 10^2$
0.15	1.00 ± 0.69	1.04 ± 0.97
0.45	0.94 ± 0.22	0.89 ± 0.38
0.75	0.58 ± 0.12	0.44 ± 0.12
1.05	0.22 ± 0.08	0.10 ± 0.06
1.35	0.09 ± 0.03	0.03 ± 0.02
1.65	0.02 ± 0.02	0.01 ± 0.02

sured from the low-mass ($M < M_c$) and the high-mass bin ($M > M_c$) as solid dots in the top and the bottom panel, respectively. As can be seen, the EE correlations of the high-mass halos are stronger at all distances than that of the low-mass halos, which implies that the EE correlations increase as the halo mass increases. This finding is also consistent with the previous results obtained for the cluster alignments by Hopkins et al. (2005).

We have also measured the EE cross-correlations, $\eta_C(r)$, between the low-mass and the high-mass halos. Basically, we select halo pairs each of which consists of one halo from the low-mass bin and one halo from the high-mass bin, and then measure the EE correlations of these halo pairs. Figure 6 plots $\eta_C(r)$ at $z = 0$ as solid dots. As can be seen, there exist significant cross-correlations between the two mass bins. Note that the EE cross-correlation is in fact stronger than the EE auto-correlation of the low-mass halos ($M < M_c$) but weaker than the EE auto-correlation of the high-mass

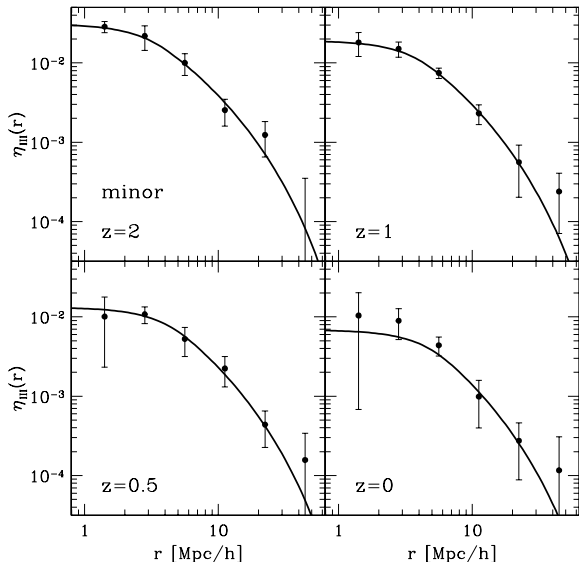


Figure 4. Same as Fig. 3 but for the case of the halo minor axes.

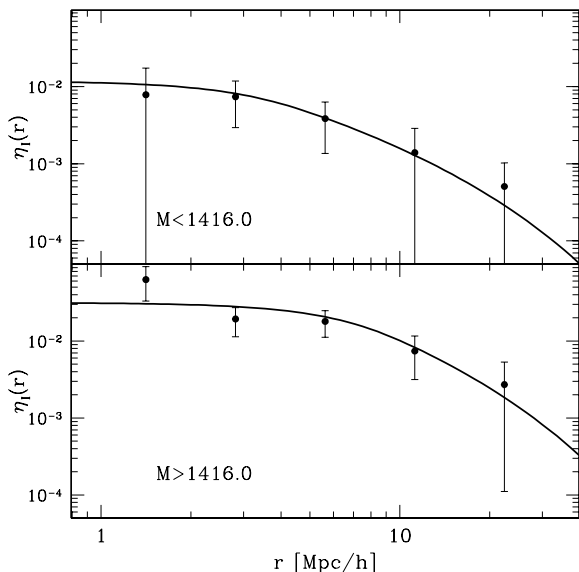


Figure 5. The EE correlations of the halo major axes measured from the low-mass ($M < M_c$) and the high-mass ($M > M_c$) bins at $z = 0$ in the top and bottom panel, respectively. The mass threshold $M_c = 1416$ is in unit of $10^{10} h^{-1} M_\odot$.

halos ($M > M_c$). This result suggests that the anisotropic merging and infall along filaments tend to increase not only the EE correlations on the same mass scale but also the EE cross-correlations between different mass scales.

3.4 Fitting formula

According to the first order linear model, the EE correlations are induced by the spatial correlations of the primordial tidal

Table 2. The EE correlations of the major axes of the low-mass and the high-mass halos.

$\log[r/(h^{-1}\text{Mpc})]$	$\eta_l(r) \times 10^2$ low-mass	$\eta_l(r) \times 10^2$ high-mass
0.15	0.78 ± 0.95	6.28 ± 2.98
0.45	0.74 ± 0.44	1.93 ± 0.79
0.75	0.38 ± 0.25	1.80 ± 0.68
1.05	0.14 ± 0.15	0.74 ± 0.42
1.35	0.05 ± 0.05	0.27 ± 0.26
1.65	0.01 ± 0.03	0.09 ± 0.07

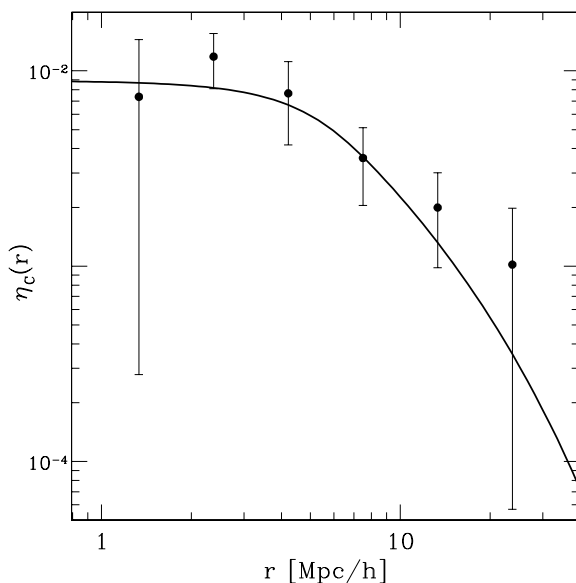


Figure 6. The EE cross-correlations of the major axes between the high and the low mass halos at $z = 0$.

field and can be approximated in the linear regime by a quadratic scaling of the linear correlation function as $\eta(r) \propto \xi^2(r)$ (Catelan et al. 2001; Lee & Pen 2001; Hirata & Seljak 2004). Since $\xi^2(r)$ decreases rapidly with separation distance r , the linear model predicts that the EE correlations exist only between close pairs with r less than a few Mpc. In other words, the large scale EE correlations cannot be described by the linear model.

Hui & Zhang (2002) pointed out that the growth of the non-Gaussianity in the density field should cause the EE correlations to scale linearly with $\xi(r)$. It indicates that the non-Gaussianity tends to increase the large-scale EE correlations. Although Hirata & Seljak (2004) discussed that the assumption of $\eta(r) \propto \xi(r)$ is valid only in the linear regime, we use here the following fitting formula for $\eta(r)$:

$$\eta(r) \approx a \tilde{\xi}_A(r). \quad (3)$$

Here a is a fitting parameter, representing the amplitude of the EE correlation, whose value is to be determined empirically. Since $\eta(r)$ is always positive and does not exceed $2/3$, the correlation parameter a is expected to be in the range of $[0, 2/3]$.

Table 3. Redshift (z), halo mean mass (\bar{M}) in unit of $10^{10}h^{-1}M_{\odot}$, number of halos (N_h), and the best-fit values of a for the EE correlations of the halo major axes.

z	\bar{M} [$10^{10}h^{-1}M_{\odot}$]	N_h	$a \times 10^2$
0	1638.15	121773	1.12 ± 0.06
0.5	1118.82	131505	2.45 ± 0.11
1	810.92	125363	2.64 ± 0.23
2	448.33	73514	3.01 ± 0.39

In eq. (3), $\tilde{\xi}(r)_A$ is the *rescaled* two-point correlation function of the linear density field, defined as

$$\tilde{\xi}_A(r) \equiv \frac{\int P(k)[(\sin kr)/kr]W^2(k; M) d^3k}{\int P(k)W^2(k; M) d^3k}, \quad (4)$$

which satisfies $\tilde{\xi}_A(0) = 1$. Here, $P(k)$ is the linear power spectrum, and $W(k; M)$ is the top-hat spherical filter corresponding to the mass scale M . We have employed the approximate formula given by Bardeen et al. (1986) for the Λ CDM power spectrum, using the same values of the cosmological parameters that were used for the Millennium Run simulation. For the shape factor Γ of the power spectrum parameterization, we adopted $\Gamma = \Omega_m h$. For the smoothing mass scale M in eq. (4), we use the mean mass averaged over the selected FOF halos.

We fit the numerical results obtained in Section 3.2 to eq. (3) by adjusting the parameter, a with the help of the maximum likelihood method (Barlow 1991). Basically, it amounts to finding the minimum of the χ^2 function defined as

$$\chi^2 = [\eta_i - \eta(r_i; a)]C_{ij}^{-1}[\eta_j - \eta(r_j; a)] \quad (5)$$

where η_i is the numerical data point at the i -th radial bin, r_i , $\eta(r_i; a)$ represents the fitting model (eq. 3) calculated at r_i , and (C_{ij}^{-1}) is the inverse of the covariance matrix, (C_{ij}) , whose component is calculated as the ensemble average over the 8 realizations (Barlow 1991):

$$C_{ij} = \langle (\eta_i - \eta_{0i})(\eta_j - \eta_{0j}) \rangle, \quad (6)$$

where η_{0i} represents the mean η_i obtained from the whole simulation box. It is worth mentioning here that the χ^2 function is expressed in terms of the inverse covariance matrix, (C_{ij}) , given that there exist non-negligible correlations between radial bins at distance scales larger than $5h^{-1}$ Mpc. In our case the number of realizations is larger than that of radial bins, the χ^2 function defined in terms of the inverse covariance matrix should be useful to find the best-fit value of a (Hartlap et al. 2007).

The uncertainty in the measurement of a is calculated as the curvature of the χ^2 function at the minimum (Bevington & Robinson 1996):

$$\sigma_a^2 = \left(\frac{\partial^2 \chi^2}{\partial a^2} \right)^{-1}, \quad (7)$$

The fitting results are summarized in Table 3 which lists the mean mass \bar{M} in unit of $10^{10}h^{-1}M_{\odot}$, the number of halos N_h , and the best-fit values of a at four different redshifts. Note that the value of a deviates from zero at all redshifts and decreases monotonically as z decreases. These results

Table 4. Mass bin, halo mean mass (\bar{M}) in unit of $10^{10}h^{-1}M_{\odot}$, and the best-fit values of a for the EE correlations of the halo major axes.

bin	\bar{M} [$10^{10}h^{-1}M_{\odot}$]	$a \times 10^2$
low-mass	545.7	0.86 ± 0.32
high-mass	4915.6	2.75 ± 0.39

quantify well how strong the EE correlations are and how they evolve with redshifts. The fitting models with these best-fit-values of a are plotted as solid line in Fig. 3. As can be seen, the fitting models are in good agreement with the numerical results (solid dots) at all redshifts. For comparison, we also try to fit the numerical results of the EE correlations of the halo major axes at $z = 0$ to the linear model proportional to $\xi^2(r)$. The linear model with the best-fit amplitude is shown as dashed line in the bottom-right panel of Fig.3. As can be seen, the linear model drops with r too rapidly to fit the large-scale EE correlations.

We also fit the EE correlations of the halo minor axes measured at four redshifts and the EE correlations of the major axes measured from two different mass bins at $z = 0$ to eq. (3) and plot the results as solid lines in Figs. 4 and 5. The EE cross-correlation of the halo major axes between different mass bins at $z = 0$ is similarly modeled as:

$$\eta_C(r) \approx a_c \tilde{\xi}_C(r). \quad (8)$$

Here a_c is a fitting parameter and $\tilde{\xi}_C(r)$ is defined as

$$\tilde{\xi}_C(r) \equiv \frac{\int P(k)[\sin kr/kr]W(k; M_1)W(k; M_2) d^3k}{\int P(k)W(k; M_1)W(k; M_2) d^3k}. \quad (9)$$

where M_1 and M_2 represent the mean mass averaged over the low-mass and the high-mass bin, respectively. The best-fit value of a_c is determined similarly by minimizing the χ^2 function. The fitting result for the EE cross-correlation is plotted as solid line in Fig. 6. As can be seen, the agreements between the numerical results and the fitting models are quite good for all cases.

4 THE ELLIPTICITY-DIRECTION CROSS CORRELATIONS OF HALOS

4.1 Definition

As mentioned in Section 1, another important correlation function for quantifying the cosmic web is the ED cross-correlation between the halo ellipticities and the large-scale density field. If the halo ellipticities are induced by the anisotropic infall and merging along the local filaments, then the orientations of the halo major axes must be preferentially aligned with the directions to the neighboring halos. This effect can be measured in terms of the ED cross-correlations between the halo orientations and the location of halo neighbors. We employ the following definition of the ED cross-correlations as

$$\omega(r) \equiv \langle |\hat{\mathbf{e}}(\mathbf{x}) \cdot \hat{\mathbf{r}}(\mathbf{x})|^2 \rangle - \frac{1}{3}, \quad (10)$$

where $\hat{\mathbf{r}} \equiv \mathbf{r}/r$ is a unit vector in the direction to a neighboring halo at separation distance of r .

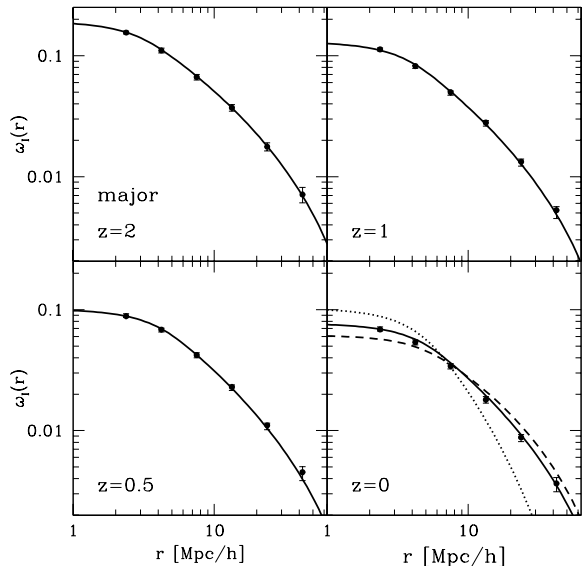


Figure 7. The ED correlations of the halo major axes (solid dots) at $z = 0, 0.5, 1$ and 2 . The errors represent the standard deviation between realizations but do not include non-negligible correlations between radial bins. In each panel the solid line represents the best-fit model with two parameters (eq. 11). In the bottom-right panel the dotted and dashed line correspond to the best-fit results based on the model with one parameter proportional to ξ and $\xi^{1/2}$, respectively.

From the halo catalogs of the Millennium Run simulation at $z = 0, 0.5, 1$ and 2 , we have measured the ED cross-correlations of the halo major (ω_I), intermediate (ω_{II}) and minor axes (ω_{III}) as a function of the comoving distance r between the halo centers. Basically, for each halo in the Millennium data at a given redshift, we find the direction to its neighbor halo and measure the separation distance r , and calculate the squares of the dot products of the normalized eigenvector with the unit vector in the direction to the neighbor halo. And then, we bin the radial distance r and calculate the mean values of $|\hat{\mathbf{e}}(\mathbf{x}) \cdot \hat{\mathbf{r}}(\mathbf{x})|^2$ averaged over those halos whose distances to the neighbor halos belong to a given bin, subtracting $1/3$ from it. We perform this procedure at $z = 2, 1, 0.5$ and 0 .

4.2 Evolution with redshift

Figure 7 plots ω_I at redshifts $z = 0, 0.5, 1$ and 2 in the top-right, top-left, bottom-right and bottom-left panel, respectively. The errors represent the standard deviation between 8 realizations. Since we are mainly interested in the cross-correlations between the halo principal axes and the large scale density field, we focus on separation scales greater than $1h^{-1}\text{Mpc}$. As can be seen, the ED cross-correlations of the halo major axes also decrease as z decreases at all distance scales. Note also that the ED cross-correlations are much stronger than the EE correlations shown in Fig. 3. The ED signal is statistically significant even at distances out to $50h^{-1}\text{Mpc}$.

The ED cross-correlations of the intermediate and minor axes of halos, ω_{II} and ω_{III} , are plotted in Figs. 8 and 9,

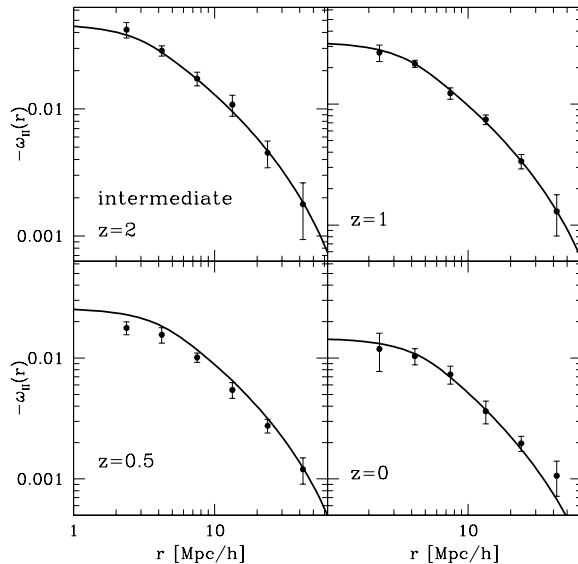


Figure 8. Same as Fig. 7 but for the case of the halo intermediate axes.

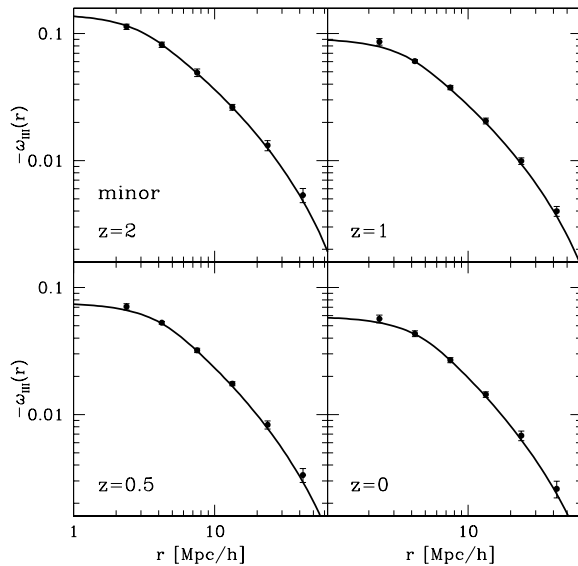
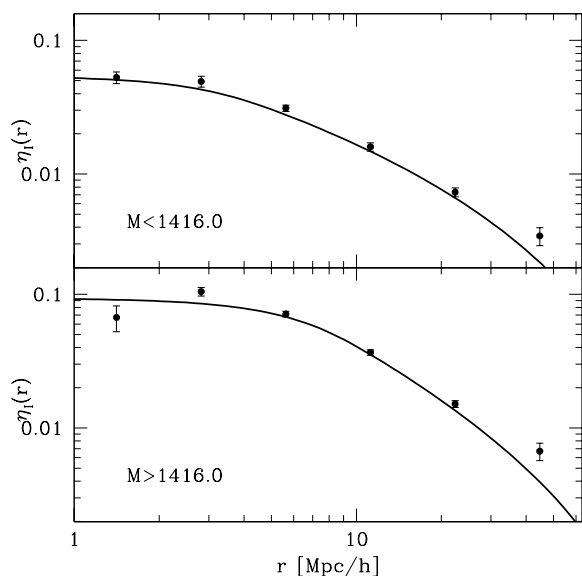


Figure 9. Same as Fig. 7 but for the case of the halo minor axes.

respectively. As expected, the intermediate and minor axes are *anti-correlated* with the directions to neighboring halos, and the degree of the anti-correlation is stronger for the minor axes. In fact, the ED anti-correlations of the halo minor axes are almost as strong as the ED correlations of the halo major axes. These results demonstrate clearly that the halo major axes preferentially point in the directions where the local density stays high, hence this gives a quantitative measure for the filamentary distribution of the halos in the cosmic web. The numerical results on ω_I , ω_{II} and ω_{III} measured at $z=0$ are summarized in Table 5.

Table 5. Numerical results for the ED cross-correlations of the halo major (ω_I), intermediate (ω_{II}), and minor (ω_{III}) axes in logarithmic scale measured at $z = 0$.

$\log[r/(h^{-1}\text{Mpc})]$	$\omega_I(r) \times 10^2$	$-\omega_{II}(r) \times 10^2$	$-\omega_{III}(r) \times 10^2$
0.375	6.85 ± 0.35	1.19 ± 0.42	5.67 ± 0.40
0.625	5.37 ± 0.26	1.04 ± 0.16	4.33 ± 0.22
0.875	3.42 ± 0.17	0.73 ± 0.12	2.68 ± 0.12
1.125	1.80 ± 0.11	0.36 ± 0.08	1.43 ± 0.07
1.375	0.88 ± 0.05	0.20 ± 0.03	0.68 ± 0.06
1.625	0.37 ± 0.04	0.11 ± 0.03	0.26 ± 0.04

**Figure 10.** The ED cross-correlations of the halo major axes measured from the low-mass ($M < M_c$) and the high-mass ($M > M_c$) bins at $z = 0$ in the top and the bottom panel, respectively. The mass threshold $M_c = 1416$ is in unit of $10^{10}h^{-1}M_\odot$.

4.3 Variation with mass

To explore how the ED correlation changes with halo mass, we measure the ED correlation of the halo major axes at two different mass bins with the mass threshold $M_c = 1.42 \times 10^{13}h^{-1}M_\odot$ at $z = 0$. When finding the neighbors, we consider all halos, no matter what mass the neighbor halos have. Figure 10 plots the ED correlations of the halo major axes at two different mass bins at $z = 0$. As can be seen, the ED correlations increase as the halo mass increases, just like the EE correlations, which suggests that the anisotropic merging contributes significantly to the ED correlations.

4.4 Fitting formula

Given the observed fact that the EE correlations scale linearly with the linear density two-point correlation function (Section 3.4), we have also tried in vain to model the ED correlations as a linear scaling of the density correlation function. But, it has turned out that this simple model fails in providing good fits to the large-scale ED cross correlations (see Fig. 7). To improve the fitting result, we need a model

which decreases with r more slowly than $\xi(r)$. We suggest the following empirical formula:

$$\omega(r) \approx b_1 \tilde{\xi}_A(r) + b_2 \tilde{\xi}_A^{-1/2}(r) \quad (11)$$

where the two parameters b_1 and b_2 lie in the range of $[-1/3, 2/3]$. The second term proportional to $\xi^{1/2}$ is included to fit the large-scale ED correlations. For the halo major-axis, both of b_1 and b_2 will have positive values, while for the halo minor and intermediate axes, they will be negative. We also expect that b_1 and b_2 will have larger values than a , since the ED cross-correlation is a more direct measure of the filamentary distribution of dark matter halos.

We fit the numerical results on the ED correlations obtained in Sections 4.2-4.3 to eq. (11) and determine the best-fit values of b_1 and b_2 by minimizing the χ^2 function:

$$\chi^2 = [\omega_i - \omega(r_i; b_1, b_2)] C_{ij}^{-1} [\omega_j - \omega(r_j; b_1, b_2)], \quad (12)$$

where ω_i is the numerical data point at the i -th distance bin, r_i , and $\omega(r_i; b_1, b_2)$ is the fitting model at r_i . The covariance matrix, (C_{ij}) , is calculated as

$$C_{ij} = \langle (\omega_i - \omega_{0i})(\omega_j - \omega_{0j}) \rangle, \quad (13)$$

where ω_{0i} is the mean ω_i obtained from the whole simulation box. To calculate errors in the measurement of b_1 and b_2 , we first construct a 2×2 curvature matrix defined as

$$\mathcal{F}_{ij} = \left(\frac{\partial^2 \chi^2}{\partial b_i \partial b_j} \right), \quad (14)$$

with $i, j = \{1, 2\}$. The errors are calculated as the diagonal components of the inverse curvature matrix (Dodelson 2003):

$$\sigma_{b_1}^2 = (\mathcal{F}^{-1})_{11}, \quad \sigma_{b_2}^2 = (\mathcal{F}^{-1})_{22}. \quad (15)$$

Table 6 lists the best-fit values of b_1 and b_2 for the ED correlations of the halo major axes measured at $z = 0, 0.5, 1$ and 2 . The best-fit value of the parameter b_2 is larger than that of b_1 at every redshift, indicating that the second term in eq. (11) dominates. The values of the two parameters decrease monotonically as z decreases, just like the EE correlations. Our results provide a quantitative description of the evolution of the ED correlations and its scaling with distance.

The fitting results on the ED correlations of ω_I , ω_{II} and ω_{III} at $z = 0$ with the best-fit values of b_1 and b_2 are plotted as solid lines in Figs. 7, 8, and 9, respectively. As can be seen, the agreements between the fitting models and the numerical results are quite good at all redshifts. For comparison, we also fit the numerical results of the ED correlations of the halo major axes at $z = 0$ to two different models proportional to ξ and $\xi^{1/2}$, which are plotted in the bottom right panel as dotted and dashed line, respectively. As can be seen, the model proportional to ξ decreases with r too rapidly to fit the numerical results. Meanwhile the $\xi^{1/2}$ decreases slowly with r but it alone still does not agree with the numerical results as well as eq. (11).

Figure 10 plots the fitting results on the ED correlations of the major axes of the low-mass and high-mass halos at $z = 0$ in the top and bottom panel, respectively. Table 7 lists the best-fit values of b_1 and b_2 for the two cases. The values of b_1 and b_2 are higher for the high-mass halos than for the low-mass halos. Note that although the fitting models work fairly well, they seem to deviate from the numerical results by

Table 6. The best-fit values of the two correlation parameters for the ED correlations of the halo major axes at four different redshifts.

z	$b_1 \times 10^2$	$b_2 \times 10^2$
0	3.06 ± 0.20	4.61 ± 0.11
0.5	4.54 ± 0.21	5.55 ± 0.12
1	5.73 ± 0.23	7.25 ± 0.10
2	7.57 ± 0.32	11.64 ± 0.16

Table 7. The best-fit parameters of the ED cross-correlations measured from two different mass bins at $z = 0$.

mass bin	\bar{M} [$10^{10} h^{-1} M_\odot$]	$b_1 \times 10^2$	$b_2 \times 10^2$
low-mass	545.7	1.39 ± 0.36	4.02 ± 0.14
high-mass	4914.35	4.94 ± 0.29	4.39 ± 0.16

more than $3\sigma_\omega$ around $30 h^{-1}$ Mpc. We think that it reflects the failure of the assumption that the ED correlations can be described in terms of the linear density correlation function.

5 SUMMARY AND DISCUSSION

In this work, by analyzing the halo data and the semi-analytic galaxy catalog from the Millennium simulations at $z = 0, 1, 0.5$ and 2 , we have measured the ellipticity-ellipticity (EE) correlations. The correlations are close to 0.01 at a distance of $1 h^{-1}$ Mpc and remain significant at distances out to $10 h^{-1}$ Mpc. The EE correlations are found to be strongest for the case of the halo major axes, and weakest for the case of the intermediate axes.

We have found that the EE correlations of all three axes decrease as z decreases. This might be due to the growth of secondary filaments at low redshifts and the beginning ‘freeze-out’ of structure growth in Λ CDM, which plays a role in randomizing the halo ellipticities. It has been also found that the EE correlation function exhibits a strong dependence on halo mass. It increases as the mass scale increases, which might be due to the dominant filamentary merging of halos on large scales. We have also calculated EE cross-correlations between halos belonging to different mass bins. Our results have shown that the EE cross-correlations between neighboring mass bins exist at a statistically significant level as well.

We have modeled the EE correlation function as a linear scaling of the linear density two-point correlation function $\xi(r)$, which is characterized by one fitting parameter, a . The value of a represents the amplitude of the EE correlations, quantifying its scaling with mass and redshift. The fitting model with the best-fit value of a has been shown to agree with the numerical results quite well at all redshifts and all mass bins.

We have also measured the cross-correlations between the halo principal axes and the directions to neighboring halos (ED) by using the same numerical data, and found that the ED cross-correlations are much stronger than the EE correlations, at all distances. Remarkably, they are de-

tected even at distances out to $50 h^{-1}$ Mpc at a statistically significant level. Just like the EE correlations, the ED cross-correlations are found to decrease as z decreases and increase as the halo mass M increases, suggesting a dominant role of anisotropic merging and infall of matter in establishing these correlations. The intermediate and the minor axes of the halos have turned out to be anti-correlated with the directions to the neighboring halos, which is consistent with alignments of the halos shapes with the orientations of the local filament.

The ED cross-correlations are, however, found to be poorly fitted by a linear scaling of $\xi(r)$. The ED cross-correlations decrease with distance much less rapidly than $\xi(r)$. To account for the slow decrease of ED cross-correlations with distance, we include an additional term proportional to $\xi^{1/2}(r)$ in the fitting model which is then characterized by two fitting parameters b_1 and b_2 . The two parameters represent the amplitudes of the two terms of the ED cross-correlations proportional to $\xi(r)$ and $\xi^{1/2}(r)$, respectively. This fitting formula has been shown to agree with the numerical results quite well at all redshifts and at all mass bins.

Nonetheless, it is worth mentioning here that our fitting formula for the ED cross-correlations is not a physical model. It is purely empirical, obtained through comparison with the numerical results. It has yet to be understood why the ED cross-correlations scale as described by our fitting formula. At any rate, we believe that our fitting formula may be useful in the future when the ED cross-correlations can be modeled by a fundamental theory.

The EE correlations and the ED cross-correlations that we have measured here provide a useful tool to statistically characterize the anisotropy and the relevant scales of the cosmic web. It will be interesting to compare the results we obtained here for the Λ CDM cosmology with observational data from large galaxy redshift surveys. The comparison of our numerical results with observational data, however, will require a modelling of the redshift space distortions as well as of two dimensional projection effects, given that in real observations what can be usually measured is the two dimensional projected major axes of the galaxies in redshift space. In future work, we plan to model these two effects on the EE and ED correlations and compare the numerical results with real observational data.

Another important application of our results lies in studies of weak gravitational lensing. The issue of a potential cross-correlation between galaxy ellipticities and the weak gravitational lensing shear (GI cross-correlations) was first raised by Hirata & Seljak (2004). They claimed that if such GI cross-correlations exist, then they would affect the weak lensing signal as another systematic contaminant whose effect is hard to control. The GI cross-correlations are expected to occur primarily due to the ED cross-correlations: If the intrinsic ellipticities of the galaxies are cross-correlated with the surrounding large-scale density field, then it will in turn lead to a cross-correlation between the gravitational lensing shear and the galaxy ellipticities. Recent observations indeed have reported detections of the GI correlation signals in low-redshift galaxy surveys (Mandelbaum et al. 2006; Hirata et al. 2007). To assess a possible systematic contamination of weak lensing due to the GI cross-correlations, it will be important first to examine

the relation between the observed GI cross-correlations and the ED cross-correlations of the cosmic web. This work will require incorporating a model for how the galaxy shapes are aligned relative to the dark matter (Heymans et al. 2006). Our future work is in this direction.

ACKNOWLEDGMENTS

The Millennium Simulation analyzed in this paper was carried out by the Virgo Supercomputing Consortium at the Computing Center of the Max-Planck Society in Garching, Germany. The simulation databases and the web application providing online access to them were constructed as part of the activities of the German Astrophysical Virtual Observatory. G.L. works for the German Astrophysical Virtual Observatory (GAVO), which is supported by a grant from the German Federal Ministry of Education and Research (BMBF) under contract 05 AC6VHA.

We thank an anonymous referee for his/her constructive report which helped us improve significantly the original manuscript. We also thank S.D.M. White for stimulating discussion and useful suggestions. J.L. is very grateful to the warm hospitality of the Max Planck Institute for Astrophysics (MPA) in Garching where this work was initiated and performed. J.L. acknowledges financial support from Korea Science and Engineering Foundation (KOSEF) grant funded by the Korean Government (MOST, NO. R01-2007-000-10246-0).

REFERENCES

- Agustsson I., Brainerd T. G., 2006, *ApJ*, 644, L25
 Allgood B., et al., 2006, *MNRAS*, 367, 1781
 Altay G., Colberg J. M., Croft R. A. C., 2006, *MNRAS*, 370, 1422
 Bardeen J. M., Bond J. R., Kaiser N., Szalay, A. S., 1986, *ApJ*, 304, 15
 Barlow R. J., 1986, *Statistics* (London : John Wiley & Sons)
 Bevington P. R., Robinson D. K., 1996, *Data Reduction and Error Analysis for the Physical Sciences* (Boston : McGraw-Hill)
 Bond J., R., Kofman L., Pogosyan D., 1996, *Nature*, 380, 603
 Catelan P., Kamionkowski M., Blandford R. D., 2001, *MNRAS*, 320, L7
 Colberg J. M., 2007, *MNRAS*, 375, 337
 Crittenden R. G., Natarajan P., Pen U. L., Theuns T., 2001, *ApJ*, 559, 552
 Crittenden R. G., Natarajan P., Pen, U. L., Theuns, T., 2002, *ApJ*, 568, 20
 Croft R. A. C., Metzler C. A., 2000, *ApJ*, 545, 561
 Croton D. J., et al. 2004, *MNRAS*, 352, 1232
 Croton D. J., Springel V., White S. D. M., De-Lucia G., Frenk C. S., Gao L., Jenkins A., Kauffmann G., Navarro J. F., Yoshida N., 2006, *MNRAS*, 365, 11
 Dodelson S., *Modern Cosmology* (San Diego : Academic Press)
 Hartlap J., Simon P., Schneider P. 2007, *A&A*, 464, 399
 Heavens A., Refregier A., Heymans C. 2000, *MNRAS*, 319, 649
 Heymans C., White M., Heavens A., Vale C., Van Waerbeke L., 2000, *MNRAS*, 371, 750
 Hirata, C. M., Seljak U., 2004, *PRD*, 70, 063526
 Hirata C. M. et al., 2004, *MNRAS*, 353, 529
 Hirata C. M. et al., 2007, *MNRAS*, 381, 1197
 Hopkins P. F., Bahcall N. A., Bode P., 2005, *ApJ*, 618, 1
 Hui L., Zhang Z., 2002, preprint [astro-ph/0205512]
 Jing Y., 2002, *MNRAS*, 335, L89
 Kulkarni G. V., Nichol R. C., Sheth R. K., Seo H. J., Eisenstein D. J., Gray A. 2007, *MNRAS*, 378, 1196
 Lee J., Kang X., Jing Y., 2005, *ApJ*, 629, L5
 Lee J. Pen U. L., 2000, *ApJ*, 532, L5
 Lee J., Pen U. L., 2001, *ApJ*, 555, 106
 Lee J., Pen U. L., 2002, *ApJ*, 567, 111
 Lee J., Pen U. L., 2007, *ApJ*, 670, L1
 Mandelbaum R., Hirata C. M., Ishak M., Seljak U., Brinkmann J., 2006, *MNRAS*, 367, 611
 Mei S., et al., 2007, *ApJ*, 655, 144
 Mo H. J., Mao S., White S. D. M., 1998, *MNRAS*, 295, 319
 Navarro J. F., Abadi M.G., Steinmetz M., 2004, *ApJ*, 613, L41
 Patiri S. G., Cuesta A. J. Prada, F., Betancort-Rijo, J., Klypin A., 2006, *ApJ*, 652, 75
 Pen U. L., Lee J., Seljak U., 2000, 543, L107
 Shandarin S. F., Yess C., 1998, *ApJ*, 505, 12
 Sahni V., Sathyaprakash B. S., Shandarin S. F., 1997, *ApJ*, 476, L1
 Sousbie T., Pichon C., Colombi S., Novikov D., Pogosyan D., 2007, *MNRAS*, 657, 30
 Springel V. et al., 2001, *MNRAS*, 328, 726
 Springel V., White S.D.M., Hernquist L., 2004, *IAU Symposium 220*, Eds. S.D. Ryder et al., San Francisco: Astronomical Society of the Pacific, p. 421
 Springel V. et al., 2005, *Nature*, 435, 629
 West M. J., 1989, *ApJ*, 347, 610
 West M. J., Willumsen C., Dekel A., 1991, *ApJ*, 369, 287
 White S. D. M., 1984, *ApJ*, 286, 38
 Zel'dovich Y. B. 1970, *A&A*, 5, 84

This paper has been typeset from a $\text{\TeX}/\text{\LaTeX}$ file prepared by the author.